Near-Infrared Optical Characteristics of Chalcogenide-Bound Nd^{3+} Molecules and Clusters

G. A. Kumar and R. E. Riman*

Department of Materials Science & Engineering, Rutgers—The State University of New Jersey, 607 Taylor Road, Piscataway, New Jersey 08854-8065

L. A. Diaz Torres

Centro de Investigaciones en Optica, Leon Gto., Mexico 37150

S. Banerjee, M. D. Romanelli, T. J. Emge, and J. G. Brennan

Department of Chemistry and Chemical Biology, Rutgers—The State University of New Jersey, 610 Taylor Road, Piscataway, New Jersey 08854-8087

Received November 30, 2005. Revised Manuscript Received February 7, 2007

The optical properties of the nanoscale neodymium ceramic cluster $(THF)_8Nd_8O_2Se_2(SePh)_{16}$ (Nd8) and molecular $(DME)_2Nd(SC_6F_5)_3$ (Nd1) were studied by optical absorption, photoluminescence, and time-resolved spectroscopy. Both complexes exhibited emission characteristic of solid-state materials with bands centered at 927, 1078, 1360, and 1843 nm for Nd8 and 897, 1071, 1347, and 1824 nm for Nd1. The observed red-shift in the absorption and emission bands of Nd8 is attributed to the increased covalency and nephelauxetic effect. Using the calculated radiative decay time, the quantum efficiency of the $^4F_{3/2} \rightarrow {}^4I_{11/2}$ transition is calculated to be 16% in Nd8 and 9% in Nd1 with corresponding stimulated emission cross sections of 3.04×10^{-20} cm^2 in Nd8 and 1.61×10^{-20} cm^2 in Nd1 that are comparable to those of solid-state inorganic systems. This efficiency is the highest reported value for "molecular" neodymium compounds. This finding, along with the novel 1.8 μm emission, is attributed to the absence of direct Nd^{3+} coordination with fluorescence quenching vibrational groups such as hydrocarbon or hydroxide groups. The direct coordination of S, Se, and F accounts for the improved fluorescence spectral properties, because these heavy anions facilitate a low phonon energy host environment for neodymium. Monte Carlo simulation permitted analysis of energy transfer processes to show the primary source of fluorescence quenching. Cross relaxation is responsible for the quenching of the $^4F_{3/2} \rightarrow {}^4I_{15/2}$ emission whereas excitation migration quenches the $^4F_{3/2} \rightarrow {}^4I_{9/2}$ emission. These processes are mediated by a dipole−dipole interaction for Nd8 and a quadrupole−quadrupole interaction for Nd1.

Introduction

Emission of light from lanthanide (Ln) ions is a fundamentally important process with a continuously expanding range of applications in contemporary electronic devices, from TV screens to lasers and optical fibers.[1−5] Control of emission intensity is often elusive, with competitive processes such as upconversion, photon splitting, or nonradiative (vibronic) quenching often detracting from ideal performance.[6] While the introduction of Ln into solid-state oxide materials has long been facile, the incorporation of near-IR emissive lanthanide ions into unconventional materials (i.e., organic polymers) remains challenging because of the intrinsic properties of Ln sources.

Of the technologically important near-IR emission sources, Nd^{3+}, Tm^{3+}, and Er^{3+} ions are the most important. The emission of erbium at 1.54 μm is used extensively in telecommunications because glass fibers are transparent to this wavelength.[7] Recently, the intense emission properties of the erbium cluster, $(THF)_{14}Er_{10}S_6(SeSe)_6I_6$ (THF = tetrahydrofuran), were described,[8] and the utility of this compound, an emissive source of Er^{3+} ions, was demonstrated.[9] A comparison of this cluster's emission properties with those of the molecular thiolate compound $(DME)_2Er$-

* Corresponding author e-mail: riman@rci.rutgers.edu.

(1) Silversmith, A. J.; Lenth, W.; Macfarlane, R. M. *Appl. Phys. Lett.* **1987**, *51*, 1997.
(2) Maciel, G. S.; de Arajuo, C. B.; Massaddeq, Y.; Aegerter, M. A. *Phys. Rev. B* **1997**, *55*, 6335.
(3) Hebert, T.; Wannermacher, R.; Lenth, W.; Macfarlane, R. M. *Appl. Phys. Lett.* **1990**, *57*, 1727.
(4) Dowing, E.; Hesselink, L.; Ralston, J.; Macfarlane, R. M. *Science* **1986**, *273*, 1185.
(5) Bhargava, R. N.; Gallaghar, D.; Hong, X.; Nurmikko, A. *Phys. Rev Lett.* **1994**, 416.
(6) *Spectroscopy of Solid State Laser Type Materials*; Di Bartolo, B., Ed.; Plenum Press: New York, 1987.
(7) Becker, P. C.; Olsson, N. A.; Simpson, J. R. *Erbium doped fiber amplifiers-Fundamentals and Technology*; Academic Press: New York, 1999.
(8) Kornienko, A.; Kumar, G. A.; Riman, R. E; Emge, T. J.; Brennan, J. G. *J. Am. Chem. Soc.* **2005**, *127*, 3501.
(9) Kumar, G. A.; Riman, R. E.; Chen, S.; Smith, D.; Ballato, J.; Banerjee, S.; Kornienko, A.; Brennan, J. *Appl. Phys. Lett.* **2006**, *88*, 091902/1.

10.1021/cm052643p CCC: $37.00
Published on Web 05/19/2007

$(SC_6F_5)_3$ (DME = 1,2-dimethoxyethane) have also been reported.[10] Subsequently, studies on heterometallic chalcogenide clusters containing Er^{3+} and Cd or Hg revealed that chalcogen-bound lanthanide ions generally appear to be highly emissive sources of near-IR radiation.[11]

Both Tm^{3+} and Nd^{3+} are alluring additions to optical fiber manufacture because they can effectively broaden the available bandwidth that can be amplified optically. Nd^{3+} is the more complicated emission source of the three, with a cascade of emission energies[6,12,13] that is either rarely (1.34 μm) or never (1.81 μm) observed from molecular Nd^{3+} sources. Of these transitions, 1.34 μm is relevant to the telecommunications window. Chemical modifications intended to enhance Nd^{3+} emission, that is, tethering Nd^{3+} to fluorescin,[14] porphyrin,[15] or terphenyl[16] sensitizers, remain a challenging synthetic goal. In this paper, we present a detailed analysis of the emission properties of two recently described,[17] highly emissive chalcogen bound Nd^{3+} compounds, $(THF)_8Nd_8O_2Se_2(SePh)_{16}$ (Nd8) and $(DME)_2Nd(SC_6F_5)_3$ (Nd1).

Experimental Section

Synthesis. Both Nd8 and Nd1 were prepared according to procedures reported in the literature.[8−11,17]

X-ray Structure Determination of Nd1. Data for Nd1 were collected on a Bruker Smart APEX CCD diffractometer with graphite monochromatized Mo Kα radiation (λ = 0.710 73 Å) at 100 K. Crystals were immersed in Paratone oil and examined at low temperatures. The data were corrected for Lorentz effects, polarization, and absorption, the latter by a multiscan (SADABS)[18] method. The structure was solved by direct methods (SHELXS86).[19] All non-hydrogen atoms were refined (SHELXL97)[20] based upon F_{obs}^2. All hydrogen atom coordinates were calculated with idealized geometries (SHELXL97). Scattering factors (f_0, f', f'') are as described in SHELXL97. Crystallographic data and final R indices are given in Table 1. ORTEP molecular structural diagrams[21] for Nd8 and Nd1 are discussed later in the manuscript (see Results and Discussion). The crystallographic details for $(DME)_2Nd(SC_6F_5)_3$ are summarized in Table 1. Complete crystallographic details are given in Supporting Information.

Table 1. Summary of Crystallographic Details for $(DME)_2Nd(SC_6F_5)_3$

empirical formula	$C_{26}H_{20}F_{15}NdO_4S_3$
fw	921.84
space group	*PT*
crystal system	triclinic
a (nm)	0.85954(5)
b (nm)	1.27731(7)
c (nm)	1.52844(9)
α (deg)	71.244(1)
β (deg)	84.394
γ (deg)	88.361(1)
V (nm^3)	1.5814(2)
Z	2
D_{calcd} (g/cm^{-3})	1.936
temperature (K)	100(2)
λ (nm)	0.071073
abs coeff (mm^{-1})	1.962
$R(F)^a$ [$I > 2\sigma(I)$]	0.0
$R_w(F^2)^a$ [$I > 2\sigma(I)$]	0.0

[a] Definitions: $R(F) = \sum||F_o| - |F_c||/\sum|F_o|$; $R_w(F^2) = \{\sum[w(F_o^2 - F_c^2)^2]/\sum[w(F_o^2)^2]\}^{1/2}$. Additional crystallographic details are given in Supporting Information.

Spectroscopy. Absorption measurements were carried out with crystalline powder dissolved in THF using a double beam spectrophotometer (Perkin-Elmer Lambda 9, Wellesley, MA) in a 1 cm cuvette using THF as the reference solvent. The emission spectra of the powdered samples were recorded by exciting the samples with an 800 nm band of a titanium−sapphire laser (Coherent, Inc., Santa Clara, CA) in the 90°-excitation geometry. The emission from the sample was focused onto a 0.55 m monochromator (Jobin Yvon, Triax 550, Edison, NJ) and detected by a thermoelectrically cooled InGaAs detector. The signal was intensified with a lock-in amplifier (SR 850 DSP, Stanford Research System, Sunnyvale, CA) and processed with a computer controlled by the Spectramax commercial software (GRAMS 32, Galactic Corp., Salem, NH). To measure the decay time, the laser beam was modulated by a chopper, and the signal was collected on a digital oscilloscope (model 54520A, 500 MHz, Hewlett-Packard, Palo Alto, CA).

Data Analysis. The radiative lifetime (τ_{rad}) of the infrared emitting state is related to the total spontaneous emission transition probability, $\sum A$, of all the transitions from an excited state ($^4F_{3/2}$ for Nd^{3+}) by $\tau_{rad} = [\sum_{j=9/2,11/2,13/2,15/2} A]^{-1}$, where A is calculated using Judd−Ofelt theory[22,23] as

$$A(i \rightarrow j) = \frac{64\pi^4}{3h(2J+1)e^2\lambda^3}\left[\frac{n(n^2+2)^2}{9}\right]\sum_{t=2,4,6}\Omega_t\langle^4I_{3/2}||U^t||^4I_j\rangle^2 \quad (1)$$

where n is the refractive index, e is the electron charge, c is the light velocity, h is Planck's constant, Ω_t are the Judd−Ofelt intensity parameters, and $||U^t||$ are doubly reduced matrix element operators corresponding to $i \rightarrow j$ transitions (From $^4F_{3/2}$ to ^4I_j where j = 9/2, 11/2, 13/2, 15/2). Matrix elements were evaluated using the standard procedure[22] and are summarized in Table 2 for the observed transitions. The three Judd−Ofelt parameters were obtained by a least-squares fitting between the experimentally measured oscillator

(10) Kumar, G. A.; Kornienko, A.; Banerjee, S.; Riman, R. E.; Emge, T. J.; Brennan, J. G. *Chem. Mater*. **2005**, *17*, 5130.
(11) Kornienko, A.; Banerjee, S.; Kumar, G. A.; Riman, R. E.; Emge, T. J.; Brennan, J. G. *J. Am. Chem. Soc*. **2005**, *127*, 14008.
(12) Kaminski, A. A. *Laser Crystals-Their Physics and Properties*; Springer: Berlin, 1989.
(13) Kaminski, A. A. *Crystalline Lasers-Physical Processes and Operating Scheme*; CRC Press: New York, 1996.
(14) Wolbers, M. P. O.; Van Veggel, F. C. J. M.; Peters, F. G. A.; Van Beelen, E. S. E.; Hofstraat, J. W.; Geurts, F. A. J.; Reinhoudt, D. N. *Chem.—Eur. J*. **1998**, *4*, 772.
(15) Beeby, A.; Dickins, R. S.; Fitzgerald, S.; Govenlock, L. J.; Parker, D.; Williams, J. A. G.; Maupin, C. L.; Riehl, J. P.; Siligardi, G. *Chem. Commun.* **2000**, 1183.
(16) Wolbers, M. P. O.; Van Veggel, F. C. J. M.; Snellink-Ruel, B. H. M.; Hofstraat, J. W.; Guerts, F. A. J.; Reinhoudt, D. N. *J. Chem. Soc., Perkin Trans. 2* **1998**, 2141.
(17) Banerjee, S.; Huebner, L.; Romanelli, M. D.; Kumar, G. A.; Riman, R. E.; Emge, T. J.; Brennan, J. G. *J. Am. Chem. Soc*. **2005**, *127*, 15900.
(18) Bruker-ASX. *SADABS*, Bruker Nonius area detector scaling and absorption correction, version 2.05; Bruker-AXS, Inc.: Madison, WI, 2003.
(19) Sheldrick, G. M. *SHELXS86*, Program for the Solution of Crystal Structures; University of Göttingen: Göttingen, Germany, 1986.
(20) Sheldrick, G. M. *SHELXL97*, Program for Crystal Structure Refinement; University of Göttingen: Göttingen, Germany, 1997.
(21) (a) Johnson, C. K. *ORTEP II*, Report ORNL-5138; Oak Ridge National Laboratory: Oak Ridge, TN, 1976. (b) Sheldrick, G. M. *SHELXTL (XP)*, version 6.14; Bruker-AXS, Inc.: Madison, WI, 2000.
(22) Judd, B. R. *Phys. Rev. B* **1962**, *127*, 750.
(23) Ofelt, G. S. *J. Chem. Phys*. **1962**, *37*, 511.

Table 2. Calculated Matrix Elements for the Observed Transitions from $^4I_{9/2}$ Ground State to Various Excited States

transition from $^4I_{15/2}$	$\|U^2\|^2$	$\|U^4\|^2$	$\|U^6\|^2$
$^4G_{9/2}$	0.0046	0.0608	0.0406
$^4G_{5/2}$	0.8979	0.4093	0.0359
$^4F_{9/2}$	0.0009	0.0092	0.0417
$^4S_{3/2}$	0.0010	0.0422	0.4245
$^4F_{5/2}$	0.0010	0.2371	0.3970
$^4F_{3/2}$	0.0000	0.2293	0.0549

strength (f_{exp})[24] and the calculated oscillator strength (f_{cal})[22,23] using the following equations.

$$f_{exp} = \frac{2mc}{\alpha_f hN\lambda^4}\int \alpha(\lambda)\, d\lambda \tag{2}$$

$$f_{cal} = \frac{8\pi^2 mc\upsilon(n^2+2)^2}{27hn(2J+1)} \sum_{t=2,4,6} \Omega_t |\langle (S,L)J||U^t||(S',L')J'\rangle|^2 \tag{3}$$

where α_f is the fine structure constant, α is the absorption coefficient of the band, h is Planck's constant, n is the refractive index of the material, λ is the wavelength of the band, $2J + 1$ is the ground state degeneracy, and N is the concentration of Nd^{3+} ions.

The quality of the fit is determined by the root-mean-square (RMS) deviation between the experimental and the theoretical values of the oscillator strengths obtained from the following expression

$$\mathrm{RMS} = \sqrt{\frac{(\sum \Delta f)^2}{(N-m)}} \tag{4}$$

where Δf is the difference between the experimental and the calculated oscillator strengths, N is the number of transitions, and m is the number of fitting parameters.

The stimulated emission cross section of the emission band is obtained with the help of the Fuchtbauer−Ladenburg equation[12]

$$\sigma_{em} = \frac{\lambda^4 A_{RAD}}{8\pi c n^2 \Delta\lambda_{eff}} \tag{5}$$

where $\Delta\lambda_{eff}$ is the effective line width of the emission band obtained by integrating over the entire emission band and dividing it by the peak fluorescence intensity.

Monte Carlo Simulations. The theory of the Monte Carlo (MC) model for nonradiative energy transfer for random/nonrandom placement of dopants in solids is reported elsewhere.[25] Here, a random placement of dopants, Nd^{3+} ions, was assumed. From X-ray crystallographic data, the site locations of Nd^{3+} in both clusters are known. By placing dopants at the actual lattice sites, the MC model calculates the energy transfer rate on the basis of the actual distances. Our analysis of the fluorescence quenching of the Nd^{3+} ions is based on such a model because in addition to the direct transfer from donors to acceptors we consider a mixture of processes, such as migration among donors or acceptors, back transfer from acceptors to donors, and upconversion processes. The procedure used in this model to analyze luminescence transients was as follows. A number of donor (D) and acceptor (A) ions were randomly placed at the corresponding lattice sites within a numerically generated crystal sample. The transfer rates for all dopants were then calculated to obtain the elements of the characteristic energy transfer matrix

$$W^k = \begin{bmatrix} W_{D1} & \cdots & W_{DN_D}^{D1} & W_{A1}^{D1} & \cdots & W_{AN_A}^{D1} \\ \vdots & \ddots & \vdots & \vdots & \ddots & \vdots \\ W_{D1}^{DN_D} & \cdots & W_{DN_D} & W_{A1}^{DN_D} & \cdots & W_{AN_A}^{DN_D} \\ W_{D1}^{A1} & \cdots & W_{DN_D}^{A1} & W_{A1} & \cdots & W_{AN_A}^{A1} \\ \vdots & \ddots & \vdots & \vdots & \ddots & \vdots \\ W_{D1}^{AN_A} & \cdots & W_{DN_D}^{AN_A} & W_{A1}^{AN_A} & \cdots & W_{AN_A} \end{bmatrix} \tag{6}$$

where the diagonal elements are defined by

$$W_{Di} = -\left[\frac{1}{\tau_{D0}} + \sum_{j}^{N_A} W_{Di}^{Aj} + \sum_{m=1,m\neq i}^{N_D} W_{Di}^{Dm}\right],$$

$$W_{Aj} = -\left[\frac{1}{\tau_{A0}} + \sum_{i}^{N_D} W_{Aj}^{Di} + \sum_{m=1,m\neq j}^{N_A} W_{Aj}^{Am}\right] \tag{7}$$

and the interaction transfer rates W_{Di}^{Aj} between the ith donor (D) and jth acceptor (A) ion, separated by a distance R, is defined by[26,27]

$$W_{Di}^{Aj} = \frac{1}{\tau_{D0}} \exp\left[\frac{2R_0}{L_0}\left(1-\frac{R}{R_0}\right)\right] + \frac{1}{\tau_{D0}}\left[\left(\frac{R_{06}}{R}\right)^6 + \left(\frac{R_{08}}{R}\right)^8 + \left(\frac{R_{010}}{R}\right)^{10} + \ldots\right] \tag{8}$$

where R_{0S} ($S = 6, 8, 10$) is known as the critical radius of interaction, and the S values of 6, 8, or 10 correspond to the dipole−dipole, dipole−quadrupole, and quadrupole−quadrupole interactions, respectively. τ_{0D} is the decay time of the donor emission in the absence of energy transfer as predicted by the J−O theory ($\tau_{0D} = \tau_{RAD}$). The free parameters for the exchange interaction are R_0 and L_0, the critical transfer distance and the effective Bohr's radius, respectively.

The microscopic individual emissions at a time t for donors and acceptors in the kth crystal sample are calculated by using

$$P_{Di}^k(t) = [\sum_{m=1}^{N_D} (\sum_{l=1}^{N_D+N_A} U_{i,l}^{k-} \exp[tT_{l,l}^k] U_{l,m}^{k+}) P_{Dm}^{k,0}] + [\sum_{n=1}^{N_A} (\sum_{l=1}^{N_D+N_A} U_{i,l}^{k-} \exp[tT_{l,l}^k] U_{l,n}^{k+}) P_{An}^{k,0}] \tag{9}$$

$$P_{Aj}^k(t) = [\sum_{m=1}^{N_D} (\sum_{l=1}^{N_D+N_A} U_{j,l}^{k-} \exp[tT_{l,l}^k] U_{l,m}^{k+}) P_{Dm}^{k,0}] + [\sum_{n=1}^{N_A} (\sum_{l=1}^{N_D+N_A} U_{j,l}^{k-} \exp[tT_{l,l}^k] U_{l,n}^{k+}) P_{An}^{k,0}] \tag{10}$$

where $U_{i,j}^{k+}$ and $U_{i,j}^{k-}$ correspond to the $[i,j]$ elements of the similarity matrix U^k and its inverse$(U^k)^{-1}$, respectively, which diagonalize $W^k = (U^k)^{-1}T^kU^k$. The $T_{l,l}^K$ are the diagonal elements of the diagonal matrix T^k. Finally, after generating a large number of crystal samples, the normalized macroscopic emissions are calculated according to equations[26]

(24) Carnall, W. T.; Hessler, J. P.; Wagner, F. *J. Phys. Chem.* **1978**, *82*, 2152.
(25) Díaz Torres, L. A.; Barbosa-Garcia, O.; Meneses-Nava, M. A.; Struck, C. W.; Di Bartolo, B. In *Advances in Energy Transfer Processes*; Di Bartolo, B., Chen, X., Eds.; World Scientific Publishing Co.: Hackensack, NJ, 2000.
(26) Forster, T. *Ann. Phys.* **1948**, *2*, 55.
(27) Dexter, D. L. J. *Chem. Phys.* **1953**, *21*, 836.

$$\phi_D(t) = \left\langle \frac{\sum_{i=1}^{N_D} P_{Di}^{k}(t)}{\sum_{i=1}^{N_D} P_{Di}^{k,0} + \sum_{j=1}^{N_A} P_{Aj}^{k,0}} \right\rangle_{\text{over } k}, \quad \phi_A(t) = \left\langle \frac{\sum_{j=1}^{N_A} P_{Aj}^{k}(t)}{\sum_{i=1}^{N_D} P_{Di}^{k,0} + \sum_{j=1}^{N_A} P_{Aj}^{k,0}} \right\rangle_{\text{over } k} \quad (11)$$

where $P_{Di}^{k,0}$ and $P_{Aj}^{k,0}$ are the initial excitation probabilities of the ith donor and jth acceptor within the kth sample at $t = 0$. All of these steps were implemented on a personal computer using a homemade toolbox developed with MATLAB software (Natick, MA).

Results and Discussion

ORTEP diagrams of the molecular structures of Nd8 and Nd1 are shown in Figure 1a,b, respectively.

Each Nd8 cluster contains four pairs of Nd ions that are unique on a crystallographic basis. The Nd pairs can be divided into three chemically distinctive sets of Ln coordination environments. Two pairs of Nd^{3+} are unique, with the first being a pair of eight-coordinate central Nd(2) (THF, O^{2-}, $2Se^{2-}$, 4μSePh), and the second being an external seven-coordinate Nd(1) that does not interact with the oxo ligands (THF, Se^{2-}, SePh, 4μSePh). The remaining two pairs of Nd-(3) and Nd(4) ions are in chemically similar coordination environments (THF, O^{2-}, Se^{2-}, 4μSePh) that differ only in the spatial distribution of the ligands, rather than ligand identities. Each Nd^{3+} coordinates a neutral THF donor. This molecule crystallizes in the monoclinic space group $P2(1)/c$. The shortest and longest separations between two Nd^{3+} atoms within an individual cluster are calculated to be 0.3786 and 0.9822 nm, respectively. The Nd^{3+} ionic concentration in the unit cell is 19.18×10^{20} ions/cm^3, which is a high value relative to rare earth doped materials ($\sim 10^{18}-10^{19}$ ions/cm^3 range).

In contrast to Nd8, Nd1 has one Nd^{3+} ion in the molecule. This neodymium is surrounded by three SC_6F_5 ligands and four oxygen donors from two DME molecules. Also, there is a weak dative interaction between the fluorine atom F(15) of one of the coordinating $-$SC6F5 groups and the Nd^{3+} ion. This molecule is triclinic with a space group of $P\bar{1}$ and a unit cell ionic concentration of 12.65×10^{20} ions/cm^3.

The room temperature absorption spectra for Nd8 and Nd1 are shown in Figure 2. In the 400$-$1000 nm region, seven f $\rightarrow$ f absorption bands of Nd^{3+} are observed that originate from the $^4I_{9/2}$ ground state to various excited states. All absorption bands are identified using the standard notations as shown in Figure 2. The strongest absorption band is observed at 582 nm. This band corresponds to the hypersensitive transition $^4I_{9/2} \rightarrow {}^4G_{5/2}$, which is typical for all Nd^{3+}-containing materials. The oscillator strength of this transition is higher in Nd8 than Nd1. Deconvolution of the absorption band at 877 nm shows multiple bands corresponding to the $^4F_{3/2}$ emitting level for Nd8. Such multiple bands were not observed for Nd1.

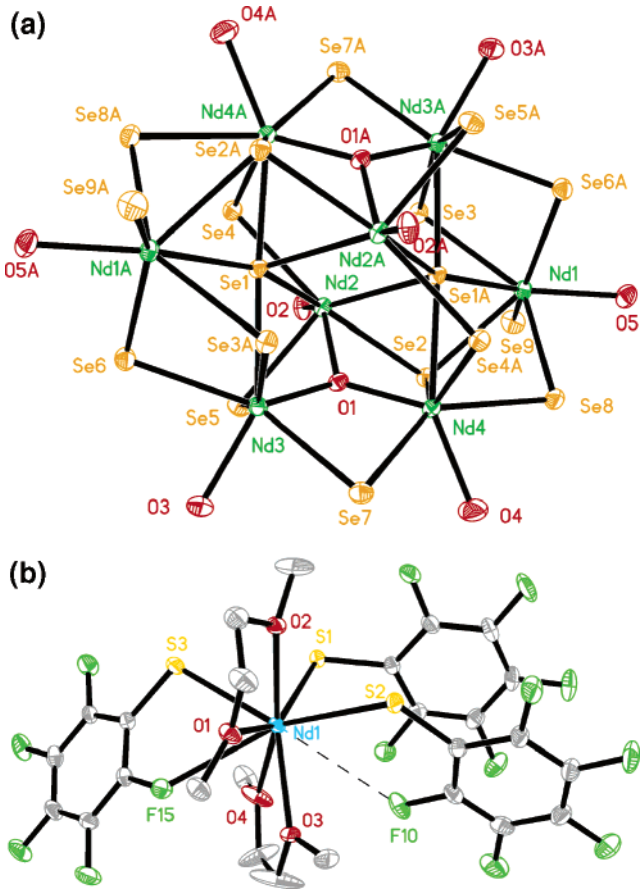

Figure 1. ORTEP diagrams for (a) $(THF)_8Nd_8O_2Se_2(SePh)_{16}$, with the C and H atoms on the oxygens (O) from the THF ligands removed for clarity, and (b) $(DME)_2Nd(SC_6F_5)_3$, also with the H atoms and C/H labels removed for clarity.

It is tempting to believe that these multiple bands may be attributed to the crystal field splitting of the $^4F_{3/2}$ emitting level. The magnitude of the crystal field splitting depends on the second-order terms of the crystal field parameters B_{20} and B_{22}. These parameters are due to asymmetric arrangements of the nearest neighbor ligands and the bond distances between Nd^{3+} ions and their nearest neighbor ligands. However, because we were unable to observe such splitting with Nd1, it is possible that crystal field splitting cannot be observed at room temperature for these compounds in general. In addition, assuming we could observe crystal field splitting, the splitting energy would correspond to 18 nm, which is more than twice that observed for amorphous materials ($\sim$8 nm).[28] It is unlikely to observe splitting energies that are much higher than those of amorphous materials, because these materials possess highly asymmetric bonding environments for Nd. Thus, a more likely source for these observed multiple absorptions rests with the three unique pairs of Nd^{3+} ions in the Nd8 cluster. Each of these three pairs contributes a unique crystal field environment and corresponding absorbance that when superimposed provide the observed multi-band structure. The use of low-temperature spectroscopy will shed more light on this because cryogenic temperatures can reveal the multi-band

(28) Iwamura, M.; Hasegawa, Y.; Wada, Y.; Murakoshi, K.; Nakshaima, N.; Yamanaka, T.; Yanagida, S. *J. Lumin.* **1998**, *79*, 29.

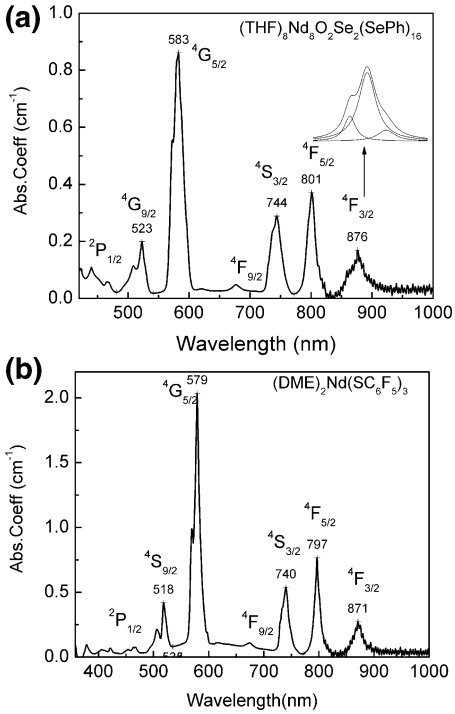

Figure 2. (a) Absorption spectrum for $(THF)_8Nd_8O_2Se_2(SePh)_{16}$ in THF at 0.0058 m concentration with the spectroscopic notations for the observed band transitions. The inset shows the deconvolution of the absorption band at 871 nm with the spectral components. (b) Absorption spectrum $(DME)_2Nd(SC_6F_5)_3$ in DME at 0.0058 m concentration with the spectroscopic notations for the observed band transitions.

Table 3. Experimentally Observed Band Positions, Their Integrated Absorbance, and Experimental and Calculated Oscillator Strengths for (a) Nd8 and (b) Nd1 Compounds[a]

transition	wavelength (nm)	$\int\alpha(\lambda)\,d\lambda$ (10^{-7})	f_{exp} (10^{-6})	f_{cal}[a] (10^{-6})
		(a) Nd8 Compound		
$^2P_{1/2}$	440			
$^4G_{9/2}$	523	4.63	0.454 ± 0.027	0.213 ± 0.012
$^4G_{5/2}$	583	18.7	1.99 ± 0.12	1.67 ± 0.10
$^4F_{9/2}$	677	1.45	0.085 ± 0.005	0.075 ± 0.004
$^4S_{3/2}$	744	6.55	0.318 ± 0.019	0.427 ± 0.025
$^4F_{5/2}$	801	7.00	0.292 ± 0.017	0.409 ± 0.024
$^4F_{3/2}$	876	6.55	0.228 ± 0.013	0.146 ± 0.008
		(b) Nd1 Compound		
$^2P_{1/2}$	440			
$^4G_{9/2}$	518	7.44	0.441 ± 0.026	0.672 ± 0.043
$^4G_{5/2}$	579	32.5	1.55 ± 0.09	1.55 ± 0.09
$^4F_{9/2}$	677	3.38	0.119 ± 0.007	0.193 ± 0.011
$^4S_{3/2}$	740	10.1	0.297 ± 0.017	0.423 ± 0.025
$^4F_{5/2}$	797	11.3	0.284 ± 0.017	0.301 ± 0.018
$^4F_{3/2}$	871	7.73	0.162 ± 0.009	0.201 ± 0.012

[a] (a) $\Omega_2 = 8.0 \pm 0.12 \times 10^{-20}$ cm^2, $\Omega_4 = 1.5 \pm 0.02 \times 10^{-20}$ cm^2, and $\Omega_6 = 1.2 \pm 0.01 \times 10^{-20}$ cm^2. RMS $= 0.256 \times 10^{-6}$. (b) $\Omega_2 = 1.1 \pm 0.01 \times 10^{-20}$ cm^2, $\Omega_4 = 1.2 \pm 0.01 \times 10^{-20}$ cm^2, and $\Omega_6 = 1.0 \pm 0.015 \times 10^{-20} \pm$ cm^2. RMS $= 0.159 \times 10^{-6}$.

absorption indicative of crystal field splitting for both Nd1 and Nd8.

All of the observed absorption bands are numerically integrated to obtain the experimental oscillator strengths, and the values obtained are summarized in Table 3(a, b) along with the observed band positions and their spectral assignments. These values are less than that of Nd^{3+} in many reported organic materials[28,29] because of the low integrated absorbance values of these complexes. The measured oscillator strengths (f_{exp}) are fitted with calculated oscillator strength (f_{cal}) values to obtain the three phenomenological intensity parameters. For Nd8, these are $\Omega_2 = 8.00 \pm 0.12 \times 10^{-20}$ cm^2, $\Omega_4 = 1.50 \pm 0.02 \times 10^{-20}$ cm^2, and $\Omega_6 = 1.20 \pm 0.01 \times 10^{-20}$ cm^2. For Nd1, the corresponding values are $\Omega_2 = 1.10 \pm 0.01 \times 10^{-20}$ cm^2, $\Omega_4 = 1.20 \pm 0.01 \times 10^{-20}$ cm^2, $\Omega_6 = 1.00 \pm 0.015 \times 10^{-20}$ cm^2, respectively. RMS values were found to be of the order of $1.59-2.56 \times 10^{-7}$cm^2, which showed that the Judd−Ofelt model was suitable in predicting the radiative spectral properties with these three fitting parameters.

The errors in the Judd−Ofelt fitting analysis depends on three factors, which include (1) the number of transitions involved in the fitting procedure, (2) the accuracy with which the oscillator strengths are evaluated, and (3) the exclusion of the hypersensitive bands. Because the experimental oscillator strength of the hypersensitive band $^4I_{9/2} \rightarrow {}^4G_{5/2}$ is comparatively higher than that of the other absorption bands, the involvement of this band results in larger error in the fitting procedure and is normally excluded, as it was in this study. The other source of error is associated with the mathematical approximations used in the derivation of the line strength. However, it is widely accepted that this theory can be applied very effectively to compute the radiative spectral properties of a rare earth ion in any matrix with an error of 15−20%.[30] This is in contrast with the systematic error found in the actual spectroscopic measurement, which is typically less than 2%.

The calculated Judd−Ofelt intensity parameters are used to evaluate the transition probability and radiative decay time for the infrared band of interest. Changes in the Judd−Ofelt parameters arise from the difference in the ligand field and bonding properties around the Nd^{3+} ion. The Ω_2 parameter is particularly sensitive to the ligand field and is more related to the covalency of the Nd^{3+}-first coordination shell interaction.[31] The Judd−Ofelt intensity parameters Ω_t depend both on the chemical environment and on the rare earth ion, and theoretically they are given by[22]

$$\Omega_t = \frac{(2t+1)\sum|A_{S,P}|^2\Xi^2(S,t)}{(2S+1)} \qquad (12)$$

where $A_{S,P}$ are the crystal field parameters of rank S and are related to the structure around the rare earth ions. $A_{S,P}$ is related to the coordination geometry and to the nature of the chemical environment around the Nd^{3+} ion and is generally expressed as[22]

$$A_{S,P} = \left(\frac{4\pi}{2t+1}\right)^{1/2} \sum_j \frac{\alpha_j}{R_j^{t+1}} Y_p^t(\theta_j,\phi_j) \qquad (13)$$

where α_j is the isotropic polarizability of the jth ligand atom or group of atoms at position R_j and Y_p^t is the spherical harmonic function of rank k. Thus, Ω_2 is affected

(29) Sun, L. N.; Zhang, H. J.; Meng, Q. G.; Liu, F. Y.; Fu, L. H.; Peng, C. Y.; Yu, J. B; Wang, S. B. *J. Phys. Chem. B* **2005**, *109*, 6174.

(30) Kumar, G. A.; Lu, J.; Kaminskii, A. A.; Ueda, K. I.; Yagi, H.; Yanagitani, T.; Unnikrishnan, N. V. *IEEE J. Quantum Electron.* **2004**, *40*, 747.

(31) Judd, B. R, J. *Chem. Phys.* **1979**, *70*, 4830.

by the asymmetry of the rare earth sites, which is reflected in the $A_{S,P}$ term in eq 13. The lower value of Ω_2 in Nd1 results from the weaker bonding of Nd^{3+} in lattice sites than for Nd8.

Ξ(S, t) is related to the matrix elements between the two radial wave functions of 4f and the admixing levels (e.g., 5d and 5g) and the energy difference between these two levels. $\Xi(S,\lambda)$ is directly proportional to the nephelauxetic parameter β,[22] which in turn is proportional to the degree of covalency of the rare earth.[32]

For Nd^{3+} the transition $^4I_{9/2} \rightarrow {}^4G_{5/2}$ is found to be hypersensitive by the selection rule ($\Delta J \geq 2$). Also, the transition $^4I_{9/2} \rightarrow {}^4F_{7/2}$ is observed to be hypersensitive to the environment. Thus, these two transitions can indicate the degree of covalency of the rare earth ligand interaction. Quantitatively this effect can be expressed by the nephelauxetic parameter β and is given by[32]

$$\beta = \frac{\nu_f - \nu}{\nu_f} \tag{14}$$

where ν_f and ν are the transition energies of the free ion and the ion in the matrix, respectively. Data for Nd ions can be found in ref 33. Because the nephelauxetic parameter is directly related to the Judd−Ofelt parameter through eq 12, an increase in the nephelauxetic parameter shows strong covalency of the Nd^{3+} with the surrounding matrix. Because the value of the Ω_2 parameter is mainly controlled by the transition matrix elements $\langle {}^4I_{9/2}||U^2||{}^4G_{5/2}\rangle$, it can be seen that Ω_2 depends entirely on the intensity of the $^4I_{9/2} \rightarrow {}^4G_{5/2}$ hypersensitive transition. Thus the values of Ω_2 are closely related to the intensity of hypersensitive transitions, that is, the larger the oscillator strength of the hypersensitive transition, the larger will be the value of Ω_2.

Another way of accounting for the covalency of the rare earth ligand bond is through the measurement of the covalency parameter[33] of the hypersensitive bands. This is obtained from the ratio I_L/I_S, where I_L and I_S are the long and short wavelength transition intensities of the Stark components of the hypersensitive bands. An increase in this ratio is found to indicate a shift of the absorption band baricenter to a longer wavelength, which in turn shows an increase in the covalency of the bond.

To account for the covalency effect on these crystals, the covalency parameter (I_L/I_S) and nephelauxetic parameter were measured. An increase in the intensity ratio (I_L/I_S) shows a shift of the center of hypersensitive absorption bands to a longer wavelength, indicating an increase in neodymium−ligand bond covalency. This red shift results from the nephelauxetic effect, which arises from the expansion of the partly filled f shell due to charge transfer from the ligands to the core of the central ion. The overlap of the ligand field with the Nd^{3+} ion reduces the values of the free ion parameters such as Slater−Condon and spin orbit interaction [following the energy matrix diagonalization procedure, we found that the Slater−Condon (F_2, F_4, F_6) and spin orbit interaction parameter (ξ4f) of Nd8 are smaller than that for Nd1] and causes a contraction of the energy level structure of the ion in the crystal matrix. Consequently this leads to a shift of the absorption and emission bands toward lower energies. Thus, by measuring the red shift of the hypersensitive bands, the degree of neodymium−ligand bond covalency can be evaluated. In the present complexes, the red shift observed for the two hypersensitive transitions are in the range 579−583 ($^4I_{9/2} \rightarrow {}^4G_{5/2}$) and 733−737 nm ($^4I_{9/2} \rightarrow {}^4F_{7/2}$). Also, the values of the nephelauxetic parameter obtained are 8.55×10^{-3} (Nd8) and 1.67×10^{-3} (Nd1). The lower value of Ω_2 in Nd1 results from the weaker bonding of Nd^{3+} in lattice sites. The increase in the peak wavelength of the hypersensitive transition for Nd8 reflects a decreasing 4f−5d energy difference, that is, ΔE. The increase is attributed to increasing polarizability of the ligands around the rare earth ions. Selenium ions have higher polarizability than fluoride ions because of the lower electronegativity. Higher ligand polarizability results in a larger overlap between rare earth and ligand orbitals, that is, a higher degree of covalency between rare earth ion and the ligands. According to the nephelauxetic effect, this leads to an expansion of the partially filled 4f shell, decreasing the repulsion between the electronic configurations of the rare earth ions. As a result the energy difference between the $4f^N$ and $4f^{N-1}5d$ configuration decreases, which in turn increases the value of Ω_2 and, thus, $\Xi(S,\lambda)$ and $A_{S,P}$ according to the expression[23]

$$\Xi(S,t) = [2\sum_{n,l}(2f+1)(2l+1)(-1)^{f+l}]\begin{Bmatrix}1 & t & s\\ f & l & f\end{Bmatrix}\begin{Bmatrix}f & 1 & l\\ 0 & 0 & 0\end{Bmatrix}\begin{Bmatrix}l & s & f\\ 0 & 0 & 0\end{Bmatrix}\frac{\langle 4f|r|nl\rangle\langle nl|r^s|4f\rangle}{\Delta E(nl)} \tag{15}$$

where the terms within the braces are 6j symbols and $\langle 4f|r^s|n'l'\rangle$ are the radial integrals

$$\int R(n,l)r^s R(n'l')\,dr \tag{16}$$

$\Delta E(nl)$ are the energy difference between the $4f^N$ and the excited $4f^{N-1}n'l'$ configuration, in this case $4f^{N-1}5d'$, and R/r is the radial part of the appropriate one electron wave function.

To measure the quantum efficiency of the $^4F_{3/2} \rightarrow {}^4I_{11/2}$ transition, the fluorescence decay time (τ_{fl}) was extracted from the measured decay curve shown in Figure 2a,b. Both decay curves were fitted with the MC model described in eqs 6−9 to yield a decay time of 186 ± 0.9 μs in Nd8 and 110 ± 0.5 μs in Nd1. Also, for Nd8, a decay time of 78 ± 0.4 μs was obtained for the 927 nm emission ($^4F_{3/2} \rightarrow {}^4I_{9/2}$), and for Nd1, a decay time of 130 ± 0.7 μs was obtained for the 1347 nm ($^4F_{3/2} \rightarrow {}^4I_{13/2}$) emission. The fitting takes into account of all the cooperative energy transfer processes between Nd^{3+} atoms located in the various crystallographic sites. Because the radiative decay time is inversely proportional to the linear combination of Ω_4 and Ω_6, the Nd1 complex shows a higher radiative decay time of 1398 μs while the corresponding value in Nd8 is 1187 μs. The experimental decay time, together with the calculated radia-

(32) Jorgenson, C. K. *Modern aspects of Ligand Field Theory*; North Holland: Amsterdam, 1971.
(33) Henrie, D. E.; Choppin, G. R. *J. Chem. Phys.* **1968**, *49*, 477.

Table 4. Fluorescence Decay Time ($^4F_{3/2} \rightarrow {}^4I_{11/2}$) and the Phonon Frequencies of Some Reported Laser Hosts

host	lifetime (μs)	phonon frequency (cm^{-1})	refs
sulfide	110	450−700	41
selenide	410	450−700	41
tellurite	233−313	450−700	42
germanate	406−550	900	41
ZBLA fluoride glass	540−610	500	41
LaF_3	800	200−400	43−45
yttrium aluminum garnet	250	400	30

tive decay time, results in calculated quantum efficiencies of 16 ± 0.2 and 9 ± 0.1% for Nd8 and Nd1, respectively. These values are the highest reported efficiencies for molecular Nd^{3+} compounds. Earlier, Hasegawa *et al*. obtained a decay time of 13 μs and a quantum efficiency of 3.2% in Nd^{3+} (bis-perfluorooctanesulfonylimide)$_3$,[34] and in all other reports[35−40] the quantum yields obtained are in the range of 10^{-2}−10^{-5}. The reported lifetimes are typical of a low phonon energy host, which is supported by Table 4 where the emission lifetimes of various classes of low phonon energy hosts are summarized and found to range from 110 to 800 μs.[30,41−45]

The emission spectra of Nd8 and Nd1 are compared in Figure 4. The characteristic Nd^{3+} emission transition scheme is shown in the inset. For Nd^{3+}, the only excited J manifold that is not relaxed predominantly by multiphonon relaxation is the $^4F_{3/2}$ state. The pump photons at 800 nm populate the $^4F_{3/2}$ excited state, and relaxation to the ^4I_J (J = 9/2, 11/2, 13/2, and 15/2) manifold yields four emission bands. The observed emission wavelengths for these compounds are 927, 1078, 1360, and 1843 nm for Nd8 and 897, 1071, 1347, and 1824 nm for Nd1. Using the three Judd−Ofelt intensity parameters and the emission spectral bandwidths the transition probabilities, fluorescence branching ratios (β), and stimulated emission cross sections are evaluated and summarized in Table 5a,b for Nd8 and Nd1. As observed in the absorption spectra the emission spectra also show considerable red shift in the Nd8 spectrum. Because the transition matrix elements $\langle {}^4F_{3/2}||U^2||^2\ {}^4I_J\rangle$ are zero for Nd^{3+} ions the Ω_2 parameter will not have any influence on the stimulated emission parameters of Nd^{3+} ions. The luminescence branching ratio can then be represented as a function of Ω_4/Ω_6 which is usually known as the spectroscopic quality factor (Q), and its value typically varies between 0.22 and 1.5.[12] Here the value of Q is 1.25 for Nd8 and 1.2 for Nd1, which are in the range of reported values. Because the values of Ω_4 and Ω_6 are comparable for Nd8 and Nd1, the fluorescence branching ratios are comparable for all the emission bands. Also the experimental branching ratios are well in agreement with the calculated values. Except for the $^4F_{3/2} \rightarrow {}^4I_{13/2}$ transition, the effective fluorescence bandwidth is higher for all bands in Nd1 than in Nd8. The inhomogeneous line width results from Stark splitting of the J manifolds, the extent of which depends on the nature of the local field, crystal field symmetry, and Nd^{3+} ionic concentrations. Thus according to expression 5 to obtain large stimulated emission cross

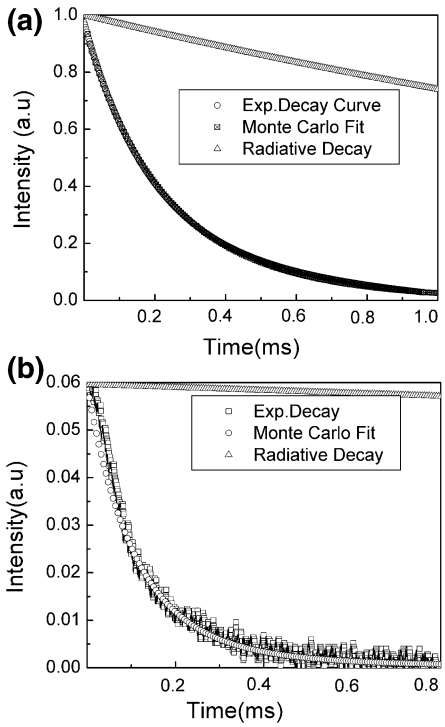

Figure 3. (a) Fluorescence decay of the $^4F_{3/2} \rightarrow {}^4I_{11/2}$ transition of Nd^{3+} in $(THF)_8Nd_8O_2Se_2(SePh)_{16}$ (circle) and the corresponding MC fit (square) assuming a dipole−dipole interaction. The upper curve (triangle) is the radiative decay corresponding to a decay time of 1187 μs. (b) Fluorescence decay of the $^4F_{3/2} \rightarrow {}^4I_{11/2}$ transition of Nd^{3+} in $(DME)_2Nd(SC_6F_5)_3$ (circle) and the corresponding MC fit (square) assuming a mixture of dipole−dipole, dipole−quadrupole, and quadrupole−quadrupole interactions. The upper curve (triangle) is the radiative decay corresponding to a decay time of 1180 μs.

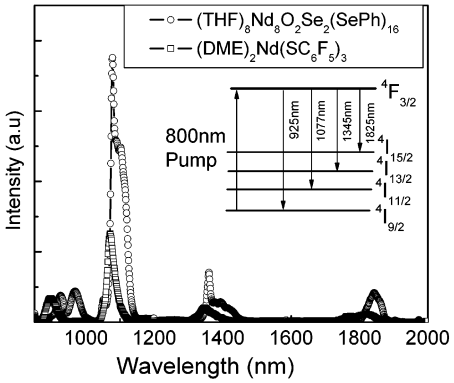

Figure 4. Comparison of the emission spectra of Nd^{3+} in the two complexes (pumping scheme and emission channels shown in the inset).

(34) Hasegawa, Y.; Ohkubo, T.; Sogabe, K.; Kawamura, Y.; Wada, Y.; Nakashima, N.; Yanagida, S. *Angew. Chem., Int. Ed.* **2000**, *39*, 357.
(35) Wolbers, M. P. O.; van Veggel, F. C. J. M.; Hofstraat, J. W; Geurts, F. A. J.; Reinhoudt, D. N. *J. Chem. Soc., Perkin Trans.* **1997**, 2275.
(36) Wolbers, M. P. O; van Veggel, F. C. J. M; Snellink-Ruel, B. H. M; Hofstraat, J. W; Geurts, F. A. J.; Reinhoudt, D. N. *J. Chem. Soc., Perkin Trans.* **1998**, 2141.
(37) Klink, S. I; Hebbink, G. A; Grave, L; van Veggel, F. C. J. M; Reinhoudt, D. N; Slooff, L. H; Polman, A; Hofstraat, J. W. *J. Appl. Phys.* **1999**, *86*, 1181.
(38) Hebbink, G. A; van Veggel, F. C. J. M.; Reinhoudt, D. N. *Eur. J. Org. Chem.* **2001**, 4101.
(39) Hasegawa, Y.; Murakoshi, K.; Wada, Y.; Kim, J. H; Nakashima, N; Yamanaka, T; Yanagida, S. *Chem. Phys. Lett.* **1996**, *248*, 8.
(40) Wada, Y.; Okubo, T.; Ryo, Munenori.; Nakazawa, T.; Hasegawa, Y.; Yanagida, S. *J. Am. Chem. Soc.* **2000**, *122*, 8583.
(41) *Optical Fiber Amplifiers-Materials, Devices, and Applications*; Sudo, S., Ed.; Artech House, Inc.: Norwood, MA, 1997.
(42) Shen, S.; Jha, A.; Zhang, E.; Wilson, S. J. *C. R. Chim.* **2002**, *5*, 921.
(43) Kaminski, A. A. *Crystalline Lasers-Physical Processes and Operating Scheme*; CRC Press: New York, 1996.
(44) Fan, T, Y; Kokta, M, R. *IEEE J. Quantum Electron.* **1989**, *25*, 1845.
(45) Stouwdam, J. W; van Veggel, F. C. J. M. V. *Nano Lett.* **2002**, *2*, 733.

Table 5. Observed Emission Bands and Their Measured and Calculated Radiative Properties for (a) Nd8 and (b) Nd1 Compounds

transition from $^4F_{3/2}$ to	wavelength (nm)	S_{ed} (10^{-20}) (cm^2)	A (s^{-1})	β_{th} (%)	β_{ex} (%)	$\Delta\lambda_{eff}$ (nm)	τ_{rad} (μs)	τ_{fl} (μs)	σ_e (10^{-20}) (cm^2)
				(a) Nd8 Compound					
$^4I_{15/2}$	1843	0.03	9	1.06	9	28	1187		0.0138
$^4I_{13/2}$	1360	0.25	142	16.8	14	39	1187		0.29
$^4I_{11/2}$	1078[a]	0.49	580	68.5	72	38	1187	186 ± 0.93	3.04
				(b) Nd1 Compound					
$^4I_{9/2}$	927	0.07	111	13.1	6	44	1187	78 ± 0.39	1.72
$^4I_{15/2}$	1824	0.03	9	1.2	13	37	1398		0.0092
$^4I_{13/2}$	1347	0.213	121	16.9	16	31	1398	130 ± 0.65	0.30
$^4I_{11/2}$	1071[b]	0.41	492	68.8	54	59	1398	111 ± 0.55	1.61
$^4I_{9/2}$	897	0.06	93	13	16	85	1398		0.71

(a) $\eta = 16.0 \pm 0.24\%$. (b) $\eta = 9.3 \pm 0.13\%$.

sections it is necessary to maximize the values of Ω_4 and Ω_6 and reduce the effective spectral bandwidth. The stimulated emission cross section obtained for the $^4F_{3/2} \rightarrow {}^4I_{11/2}$ transition in Nd8 and Nd1 are 3.0×10^{-20} and 1.6×10^{-20} cm^2, respectively, and are comparable to many well-known laser hosts.[12,43]

To understand the mechanisms of fluorescence quenching the fluorescence decay was analyzed using the MC energy transfer model. The nature of the multipolar interaction responsible for the energy transfer was understood by extracting the energy transfer function $P(t)$ from the experimental decay. According to the Forster−Dexter model[26,27] the transfer function is defined by

$$P(t) = \frac{C_A}{C_0}\Gamma\left[1 - \frac{3}{S}\right]\left(\frac{t}{\tau_{0D}}\right)^{3/S} \quad (17)$$

where $C_0 = 3/(4\pi R_{0S}{}^3)$ is the critical concentration defined through the critical transfer distance R_{0S}, with $s = 6$, 8, and 10, and Γ is the gamma function. In the log−log scale $P(t)$ is represented by a straight line with a slope of $3/s$. The transfer function shows the induced deviation from the exponential decay due to the energy transfer process; that is, the experimental decay can be expressed as follows:

$$I_D(t) = I_0 \exp\left(-\frac{t}{\tau_{0D}}\right)\exp(-P(t)) \quad (18)$$

where τ_{0D} is the radiative decay time in the absence of energy transfer and the corresponding radiative decays are shown in Figure 3a,b with the Δ symbols for Nd8 and Nd1. The energy transfer function $P(t)$ is plotted as a function of time in the log−log plot in Figure 5a,b for Nd8 and Nd1, respectively. For Nd8 the curve can be fitted with two straight lines; the first with a slope of $s = 3/6$ up to $t = 400$ μs and the rest of the curve with a slope of 1. The region with $s = 3/6$ shows that the energy transfer is predominantly by a dipole−dipole interaction, and hence the dipole−dipole interaction was assumed for the MC simulation of the decay curve in Nd8. Results of the simulations show a best fit with the experimental decay curve corroborating the fact that the dipole−dipole interaction is the driving mechanism responsible for the energy transfer in Nd8, and the critical separation for the dipole−dipole interaction is estimated to be 1 nm. Because the shortest separation between two Nd^{3+} atoms in Nd8 (0.38 nm) is less than this distance, there is always a multi-polar interaction between them to quench fluorescence emissions. On the other hand, the longest separation is 0.98 nm between Nd^{3+} atoms located at Nd(1) and Nd(1A) lattice positions. This distance is comparable to the critical separation beyond which the dipole−dipole interaction between this pair is minimal. Thus, these pairs will contribute the fluorescence intensity in Nd8. The region with slope = 1 indicates that at longer periods of time energy transfer is dominated by migration. The slope variation indicates an energy transfer transition from an initial dipole−dipole interaction at a very early time (<400 μs) toward a process dominated by a migration at a later time (>400 μs). The critical separation for the latter process is estimated to be $R_{06} = 2.7$ nm.

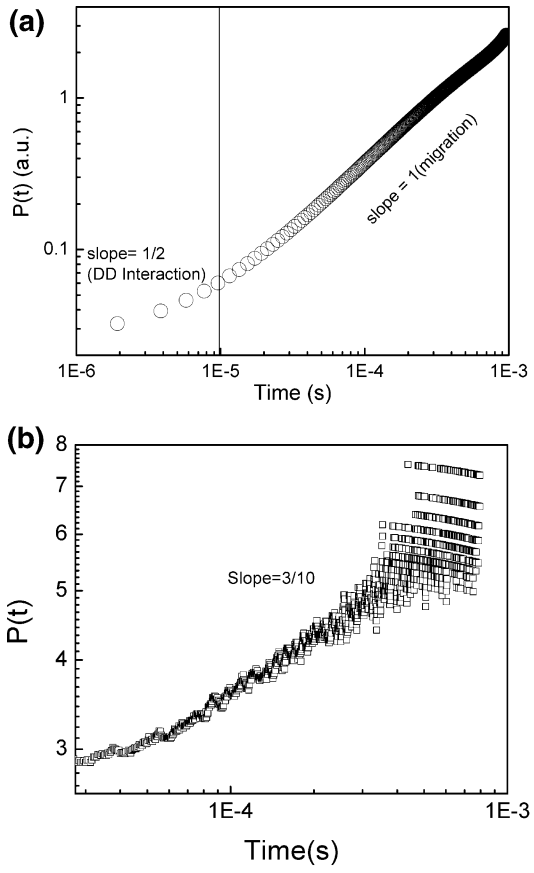

Figure 5. (a) Experimental energy transfer function of the $^4F_{3/2} \rightarrow {}^4I_{11/2}$ decay of Nd^{3+} in $(THF)_8Nd_8O_2Se_2(SePh)_{16}$. The two slopes on the temporal window show the evolution of energy transfer from dipole−dipole (DD) to a migration process at a later time. (b) Experimental energy transfer function of the $^4F_{3/2} \rightarrow {}^4I_{11/2}$ decay of Nd^{3+} in $(DME)_2Nd(SC_6F_5)_3$. The slope, $s = 3/10$, shows the predominance of a quadrupole−quadrupole interaction-mediated energy transfer process.

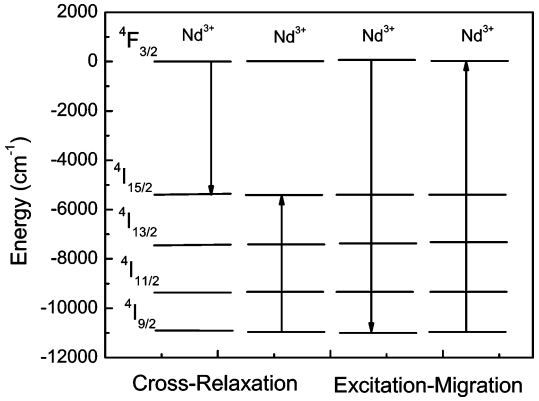

Figure 6. Schematic representation of cross relaxation and excitation migration mechanisms quenching the Nd^{3+} $^4F_{3/2}$ fluorescence.

In Nd1, the log−log plot of $P(t)$ versus t yields a slope of $s = 3/10$, indicating that the dominant interaction is quadrupole−quadrupole. For medium and longer times the MC simulation shows the best fit for the experimental decay when dipole−dipole and dipole−quadrupole (multipolar) interactions are taken into account. Thus it is assumed that in Nd1 the energy transfer is driven by a mixture of the three interactions and the critical transfer distances obtained for these interactions are $R_{06} = 1.05$, $R_{08} = 0.99$, and $R_{010} = 0.93$ nm. The little initial deviations between the MC fit and the experimental decay curve of Nd1 are due to the weak coupling to the detection system during the decay measurement.

Cross relaxation and excitation migration are mechanisms that can cause the multipolar interaction between nearby Nd^{3+} ions (Figure 6). For cross relaxation, the excitation energy that is initially localized in one ion is transferred to a nearby unexcited ion thereby leaving both of them in the same average energy state. For Nd^{3+}, this process occurs through the interaction between $^4F_{3/2}$,$^4I_{15/2}$, and $^4I_{9/2}$ levels and is represented by $^4F_{3/2} + {}^4I_{15/2} \rightarrow {}^4I_{15/2} + {}^4I_{9/2}$. Cross relaxation mainly influences the emission intensity of the $^4F_{3/2} \rightarrow {}^4I_{15/2}$ transition. For excitation migration, the probability of fluorescence quenching is increased by the movement of excitations from one location to another and finally to a trap site where it is fully quenched. For Nd^{3+}, this process occurs through the interaction between similar levels as cross relaxation but is represented instead as $^4F_{3/2} + {}^4I_{9/2} \rightarrow {}^4I_{9/2} + {}^4F_{3/2}$. Both cross relaxation and excitation migration are mediated by multipolar interactions, and according to the Forster−Dexter theory, the critical separation for these mechanisms is given by refs 26 and 27 as follows:

$$R_0^{\,6} = \frac{3h^4c^4}{4\pi n^4} Q_A \int \frac{f_S(E)\, f_A(E)\, dE}{E^4} \quad \text{(dipole−dipole)} \tag{19}$$

$$R_0^{\,8} = \frac{135\pi h^9 c^8 Q_A}{4n^6} \int \frac{f_S(E)\, f_A(E)\, dE}{E^8} \quad \text{(dipole−quadrupole)} \tag{20}$$

$$R_0^{\,10} = \frac{225\pi h^{11} c^{10}}{2n^6} \int \frac{f_S(E)\, f_A(E)\, dE}{E^{10}} \quad \text{(dipole−quadrupole)} \tag{21}$$

where $f_S(E)$ and $f_A(E)$ are the normalized line shape functions of the sensitizer emission and acceptor absorption spectra (here both sensitizer and acceptor are the same), n is the refractive index of the material, Q_A is the oscillator strength of the absorption band of the acceptor, which is in resonance with the sensitizer emission transition, and E is the average energy of the overlapping transition. Thus the strength of the energy transfer depends directly on the overlapping integral of the interacting ions and inversely on the separation between them.

In addition to concentration quenching, the major factor reducing the fluorescence quantum yield in Nd^{3+} systems is multiphonon emission through vibrational relaxation by chalcogenide bonds and nearby organic ligands. For Nd^{3+} ions, one principal channel for nonradiative multiphonon relaxation is through the $^4F_{3/2} \rightarrow {}^4I_{15/2}$, transition, which is emitting at 1843 nm. The energy gap of this band in the present Nd complexes is 5368 cm^{-1}. Thus, assuming the highest vibrational frequency of Nd−Se is 400 cm^{-1},[46] 15 phonons are required to bridge the $^4F_{3/2} \rightarrow {}^4I_{15/2}$ energy gap. The probability of phonons bridging this energy gap is very low, which means that the $^4F_{3/2} \rightarrow {}^4I_{15/2}$ transition is radiative. For this same reason, chalcogenide hosts for Nd^{3+} have been observed to emit at 1.8 μm.[47] This is in contrast to other high phonon energy oxide hosts for Nd^{3+}, where the band at 1843 nm has not been observed.[47]

For these materials, the disappearance of the 1843 nm band is due to both the influence of the multiphonon relaxation as well as the energy transfer assisted by the cross relaxation involving $^4F_{3/2}$,$^4I_{9/2}$, and $^4I_{15/2}$ levels. Because the influence of the energy transfer depends on the lattice locations of the Nd^{3+}, different hosts show different degrees of fluorescence quenching. In addition, the nearest neighbor coordination number of Nd is different between these two hosts. For evaluating the influence of phonon energy, it is important to consider the bonding of oxygen about neodymium. In Nd8, there are two central oxygen atoms with trigonal planar geometry with each of them coordinated with three neodymium atoms to form Nd−O bonds. Because of the threefold Nd^{3+} coordination, the Nd−O coordination sphere is structurally different from the coordination sphere found in oxides such as as Nd_2O_3 or YAG. In these cases, the oxygen atom is tetragonally coordinated by Nd^{3+}. We believe that a higher oxygen coordination sphere, such as O1-bonded Nd(3) in Nd8, leads to high phonon energies (e.g., 1200 cm^{-1} for an oxide host). This difference in phonon energy is sufficient to quench many infrared emissions, which includes the 1843 nm band. For example, for 1843 nm, only 5 phonons would be required to bridge the $^4F_{3/2} \rightarrow {}^4I_{15/2}$ transition.

Both O−H (3450 cm^{-1}) and C−H (2950 cm^{-1}) functional groups are also potential quenchers of Nd^{3+} emission in many

(46) Berg, D. J.; Burns, C. J.; Andersen, R. A.; Zalkin, A. *Organometallics* **1989**, *8*, 1865.
(47) *Rare Earth Doped Fiber Lasers and Amplifiers*; Digonnet, M. J. F., Ed.; Marcel Dekker, Inc.: New York, 1993.

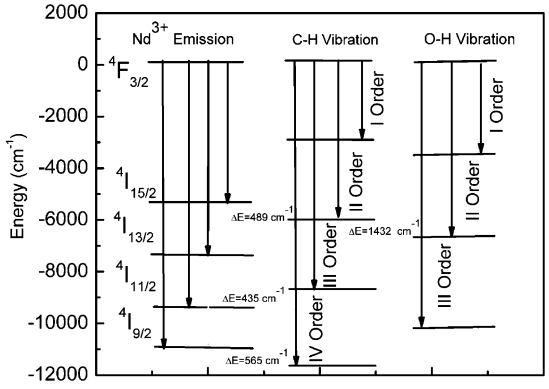

Figure 7. Schematic representation of the vibrational quenching of the $^4F_{3/2}$ emission in Nd^{3+} by the vibrational modes of C−H and O−H functional groups.

organic compounds. The $^4F_{3/2} \rightarrow {}^4I_{15/2}$ energy gap matches with the vibration modes of OH (3400 cm^{-1}) and CH (2950 cm^{-1}) as shown in Figure 7 and hence both can contribute to the efficient nonradiative deactivation of the $^4F_{3/2}$ level. The quenching due to overtones of the CH band is prominent for the $^4F_{3/2} \rightarrow {}^4I_{15/2}$, $^4I_{11/2}$, and $^4I_{9/2}$ emission bands whereas OH mostly influences the $^4I_{13/2}$ band. In the present compounds O−H is completely absent, and C−H is present, but in an apparently limited sense as observed from the infrared absorption spectra. In the fluorinated thiolate, C−H units are found only on the DME ligand that coordinates weakly though Nd−OR_2 bonds. In Nd8, there are C−H bonds in the weakly bound THF ligand and in the Ph (Se) ligands encapsulating the cluster core. The SePh are also considered to be weakly bound to Nd and distanced from Nd by relatively long Nd−Se bond lengths. It seems reasonable to assume that the multitude of SePh ligands has detracted from optimal quantum efficiency. Elimination of SePh ligands will presumably improve quantum efficiency.

With direct coordination of Nd^{3+} to heavier atoms, the coupling between the energy levels is less efficient and the Frank−Condon factor [17] for the relaxation process is reduced, effectively increasing the lifetime. Thus, both compounds are highly emissive in the near-IR spectrum, particularly when compared to the current literature.

Absolute relationships that correlate structure and fluorescence spectral properties are still elusive. With proper energy transfer and crystal field modeling, it is possible to design a structure with optimal performance characteristics, but unfortunately the experimental realization of such systems is difficult because of chemical and thermodynamic stability requirements that control phase formation in the system. In the present Nd experiments, the fluorinated thiolate compound Nd1 is shown to be the most emissive monometallic Nd compound reported to date, and cluster Nd8, with a significant number of hydrocarbon functionalized selenolate ligands, has even brighter emission properties. Nd8 has the highest quantum efficiency reported for a molecular Nd compound. Further developments in the areas of oxo and non-oxo clusters are currently under investigation.

Conclusions

The chalcogen bound Nd compounds $(THF)_8Ln_8O_2Se_2(SePh)_{16}$ and $(DME)_2Nd(SC_6F_5)_3$ show 9−16% quantum yield of emission at 1077 nm which is comparable to that of inorganic hosts. These are the highest efficiencies for molecular Nd compounds reported to date. The superior performance of this compound class is attributed to the absence of high-frequency vibrational groups such as C−H and O−H in the core and the direct link of Nd with heavy elements such as Se and S.

Acknowledgment. We would like to acknowledge the support of NSF (CHE-0303075), The New Jersey State Commission on Science and Technology, USR Optonix, Sunstones, Inc., and the U.S. Army through the South Carolina Research Authority (sub-recipient agreement 2001-509, task order 0007, Active Coatings Technology program) for their generous support.

Supporting Information Available: Crystal data and structure refinement, atomic coordinates and equivalent isotropic displacement parameters, bond lengths and angles, anisotropic displacement parameters, hydrogen coordinates and isotropic displacement parameters, and torsion angles for $C_{152}H_{192}Nd_8O_{16}Se_{18}$ and $(DME)_2Nd(SD_6F_5)_3$ (PDF). This material is available free of charge via the Internet at http://pubs.acs.org.

CM052643P